Energetic neutral atom imaging of the lunar surface

A. Vorburger,[1] P. Wurz,[1] S. Barabash,[2] M. Wieser,[2] Y. Futaana,[2] C. Lue,[2]
M. Holmström,[2] A. Bhardwaj,[3] M. B. Dhanya,[3] and K. Asamura[4]

Received 28 November 2012; revised 8 May 2013; accepted 9 May 2013; published 1 July 2013.

[1] Since the Moon is not shielded by a global magnetic field or by an atmosphere, solar wind plasma impinges onto the lunar surface almost unhindered. Until recently, it was assumed that almost all of the impinging solar wind ions are absorbed by the surface. However, recent Interstellar Boundary Explorer, Chandrayaan-1, and Kaguya observations showed that the interaction process between the solar wind ions and the lunar surface is more complex than previously assumed. In contrast to previous assumptions, a large fraction of the impinging solar wind ions is backscattered as energetic neutral atoms. Using the complete Chandrayaan-1 Energetic Neutral Analyzer data set, we compute a global solar wind reflection ratio of 0.16 ± 0.05 from the lunar surface. Since these backscattered neutral particles are not affected by any electric or magnetic fields, each particle's point of origin on the lunar surface can be determined in a straight-forward manner allowing us to create energetic neutral atom maps of the lunar surface. The energetic neutral atom measurements recorded by the Chandrayaan-1 Energetic Neutral Analyzer cover $\sim$ 89% of the lunar surface, whereby the lunar farside is almost completely covered. We analyzed all available energetic neutral atom measurements recorded by the Chandrayaan-1 Energetic Neutral Analyzer to create the first global energetic neutral hydrogen maps of the lunar surface.

Citation: Vorburger, A., P. Wurz, S. Barabash, M. Wieser, Y. Futaana, C. Lue, M. Holmström, A. Bhardwaj, M. B. Dhanya, and K. Asamura (2013), Energetic neutral atom imaging of the lunar surface, *J. Geophys. Res. Space Physics*, *118*, 3937–3945, doi:10.1002/jgra.50337.

1. Introduction

[2] Several processes can lead to the release of low energy neutral atoms (LENAs), which have energies in the range of a few eVs to 1000 eV [*Wurz*, 2000], from the lunar surface: (1) ion sputtering of material on the surface by precipitating solar wind ions, (2) backscattering of neutralized precipitating solar wind ions, (3) photon-stimulated desorption, and (4) micrometeoroid impact vaporization. Except for times when frequent meteoroid showers occur, the mass flux of meteoritic in-fall is relatively low, and thus, the flux of emitted material is low [*Wurz et al.*, 2007]. Also, the typical energy per atom is low (0.34 eV according to *Wurz and Lammer* [2003]) in comparison to the typical energy per atom generated by ion sputtering or backscattering. Micrometeoroid impact vaporization is therefore a minor contributor to the lunar LENAs. Photon-stimulated desorption occurs much more regularly for selected species, but the typical energy of particles due to photon-stimulated desorption is close to the binding energy [*Wurz and Lammer*, 2003] and outside the energy range of the data analyzed for this study. This process is therefore not a main contributor to the lunar LENAs, either. The two main processes involved in the production of lunar LENAs are thus solar wind sputtering and backscattering. The types of LENAs released through these two processes are not only of different composition but also exhibit different characteristic energies. While LENAs from backscattering should resemble the impinging solar wind composition ($\sim$ 95% H atoms and $\sim$ 5% He atoms as well as traces of heavier species) [see *Wurz*, 2005, and references therein], the sputtered particles mainly resemble the chemical composition of the lunar regolith ($\sim$ 60% O, $\sim$ 16% Si, $\sim$ 10% Al, $\sim$ 5% Mg, $\sim$ 5% Ca, $\sim$ 2.5% Fe, $\sim$ 0.4% Na, and $\sim$ 1.1% other species) [*Wurz et al.*, 2007], and the typical energy per atom is much higher for the backscattered particles than for the sputtered particles. Both processes have in common, though, that the released LENAs are a result of impinging solar wind ions.

[3] Until recently, the generally accepted assumption about solar wind ions that impinge onto the lunar surface was that almost all ions are absorbed [see *Wieser et al*., 2009, and references therein]. *Crider and Vondrak* [2002], for example, assumed that almost 99% of the incident protons are absorbed and that only 1% of the particles are backscattered and 0.1% are sputtered. This assumption has been

[1]Physikalisches Institut, University of Bern, Bern, Switzerland.
[2]Swedish Institute of Space Physics, Kiruna, Sweden.
[3]Space Physics Laboratory, Vikram Sarabhai Space Center, Trivandrum, India.
[4]Institute of Space and Astronautical Science, Sagamihara, Japan.

Corresponding author: A. Vorburger, Physikalisches Institut, University of Bern, Sidlerstrasse 5, CH-3012 Bern, Switzerland. (vorburger@space.unibe.ch)

2169-9380/13/10.1002/jgra.50337

invalidated by the recent observations made by the Interstellar Boundary Explorer (IBEX) and by Chandrayaan-1 (CH-1). Using IBEX observations, located at a distance of tens of lunar radii, *McComas et al.* [2009], *Rodríguez et al.* [2012], and *Saul et al.* [2013] have derived an average global energetic neutral atom (ENA) albedo of ∼0.10, while *Wieser et al.* [2009] and *Futaana et al.* [2012] presented a backscatter value of ∼0.20 computed from CH-1 observations in a low-altitude lunar orbit.

[4] The energy of these backscattered LENAs of solar wind origin is much higher than the escape energy. Therefore, the gravitational potential does not affect their trajectory significantly. In addition, the backscattered particles are not affected by any electromagnetic field, since they are neutralized upon interaction with the lunar surface before being scattered back to space. The particles can thus be assumed to travel along straight-line trajectories. ENAs measured by an instrument in orbit around the Moon can therefore be mapped back onto the surface in a straight-forward manner. A huge advantage of mapping backscattered particles, besides the simplicity, is that it is possible to map shadowed regions with high accuracy, because, in contrast to sunlight, solar wind ions are able to reach such regions due to their finite gyroradius, the kinetic temperature, and the pressure gradient between the solar wind and the wake region. In addition, wake formation can cause solar wind protons to be diverted toward shadowed crater floors, which has recently been demonstrated by *Zimmerman et al.* [2011] who investigated the plasma environment within a shadowed polar crater using the first fully two-dimensional kinetic simulations of plasma expansion in the vicinity of a charge-collecting surface.

[5] The analysis of first lunar ENA measurements conducted by the IBEX and the CH-1 missions showed that the solar wind ion - lunar surface interaction is more complex than previously thought. At magnetic anomalies, the interaction is even more complex, and the formation of minimagnetospheres on the lunar surface has been observed [*Wieser et al.*, 2010], which is still not fully understood. Since the proton gyroradius is large compared to the extension of most minimagnetospheres on the lunar surface, the protons should only be slightly deflected. However, *Wieser et al.* [2010], *Saito et al.* [2010], *Lue et al.* [2011], and *Vorburger et al.* [2012] showed that at the locations of magnetic anomalies, the protons are strongly affected by the magnetic field and associated plasma features. Since the magnetic anomaly provides an obstacle to the impinging solar wind ions, fewer ions are backscattered from that region than from unmagnetized regions; i.e., the location of the magnetic anomaly appears darker in a map of backscattered ENAs [*Wieser et al.*, 2010; *Vorburger et al.*, 2012]. Understanding of this process is necessary, for example, when space weathering of the lunar surface is being studied. It has been suggested that since fewer particles reach regions of high magnetic field strength, these regions are not as weathered as regions that are not protected by a minimagnetosphere [see *Blewett et al*., 2011, and references therein]. To better understand the interaction between the solar wind ions and the lunar surface, one should study the solar wind ion - lunar surface interaction on a global scale and not limit the investigation to a few selected locations. We therefore conducted a complete analysis of all Chandrayaan-1 Energetic Neutral Analyzer (CENA) data sets to create the first global ENA albedo maps of the lunar surface.

2. Instrumentation and Data Set

[6] For this analysis, we used data recorded by the Sub-keV Atom Reflecting Analyzer (SARA) [*Bhardwaj et al.*, 2005; *Barabash et al.*, 2009] on board the Chandrayaan-1 spacecraft [*Goswami and Annadurai*, 2009]. SARA consists of two sensors: the Solar Wind Monitor (SWIM) [*McCann et al.*, 2007] and the Chandrayaan-1 Energetic Neutral Analyzer (CENA) [*Kazama et al.*, 2007]. Both sensors are mass spectrometers, SWIM measures ions, and CENA measures neutrals. Together, these two sensors are able to investigate the interaction process between the solar wind ions and the lunar surface: When impinging solar wind ions hit the lunar surface, they become neutralized and are scattered back as ENAs, which can be measured by CENA. To create the backscattered ENA maps, we analyzed all ENAs measured by CENA from the complete energy range covered by CENA. CENA has 15 logarithmically spaced, slightly overlapping energy bins with center energies from 11 eV to 2.2 keV. The lower and upper bounds of the complete energy range, henceforth called effective energy range, lie at 7 eV and 3.52 keV, respectively. CENA consists of seven angular sectors that provide information about the direction of arrival. The seven angular sectors are arranged symmetrically (three on each side) around sector 3, the nadir-pointing sector. For this analysis, only measurements from the central five sectors (sectors 1–5) were used, since the two outermost sectors' fields-of-view partially include the lunar limb and space. An illustration of the arrangement of these five central sectors can be found in *Wieser et al.* [2010]. CENA is capable of mass discrimination. In this study, we only used the hydrogen channel. Analysis of data for higher mass species will be subject of a later study.

[7] CENA was in operation during 73 days intermittently between the end of January 2009 until the end of July 2009. Over that period of time, CENA conducted measurements during 328 polar orbits, 111 of which were performed at an altitude of 100 km and 217 of which were recorded at an altitude of 200 km. From these 328 orbits, 153 were usable for this analysis (47 recorded at 100 km and 106 recorded at 200 km). The other orbits had to be excluded due to one of the following reasons: The Moon was in the magnetosheath or in the magnetotail, the data were contaminated by ultraviolet light, the energy setting changed during the orbit (close to equator crossing), or the recording time of the data were insufficiently long (latitude coverage insufficient for quantitative analysis). During one observation period, coronal mass ejections occurred. The data sets recorded during this event were excluded from the mapping procedure but not from the reflection ratio computation.

3. Reflection Ratio

[8] The percentage of solar wind ions that are backscattered from the lunar surface as neutrals is called the reflection ratio. We define the reflection ratio for perpendicular solar wind incidence, $R_\perp$, by the following equation:

$$R_\perp = \frac{J_{\mathrm{ENA}}}{J_{\mathrm{SW}}}, \tag{1}$$

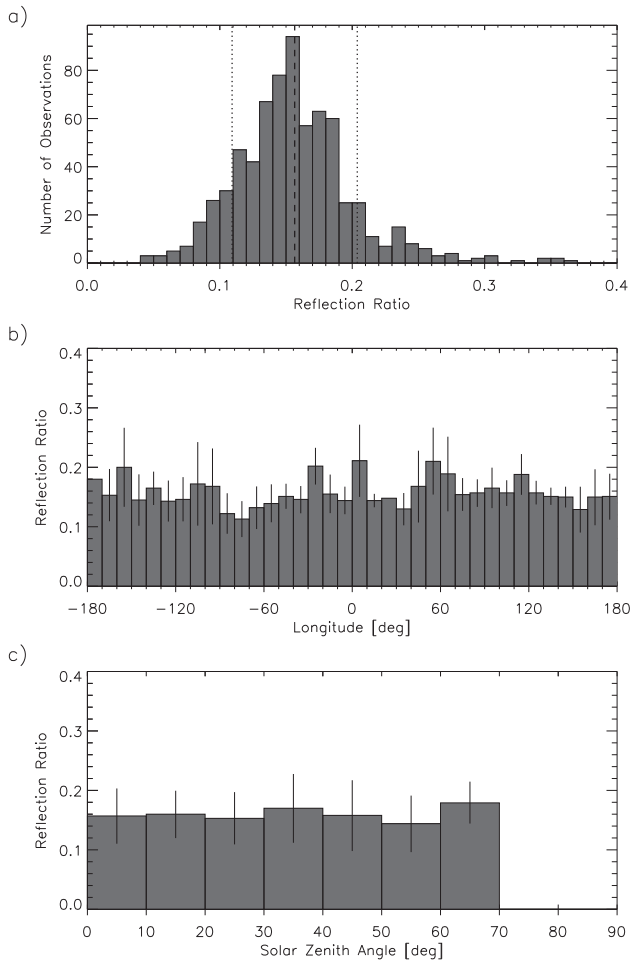

Figure 1. Reflection ratios for perpendicular incidence computed from 717 data sets. Figure 1a shows the density histogram with a mean value of 0.16 (dashed line) and a standard deviation of 0.05 (dotted lines). Figure 1b shows the mean reflection ratio versus lunar longitude. The bin-size is set to 10°, and for each bin also, the standard deviation is given where available. Figure 1c depicts the mean reflection ratio versus solar zenith angle. Again, the bin-size is set to 10°, and for each bin also, the standard deviation is given where available. In the CENA data set, the solar zenith angle was never larger than 70%.

where J_{ENA} is the total ENA flux backscattered from the surface and J_{SW} is the impinging solar wind flux observed at the Moon. For solar wind flux impinging nonperpendicular to the surface, J_{SW} has to be replaced by $J_{SW} \cdot \cos(SZA)$, with SZA being the solar zenith angle. The directional dependence of the ENA flux is described by the scattering function f_S, which is given in section A. The scattering function for lunar ENAs was first presented in *Schaufelberger et al.* [2011]. It was computed from CENA observations, which had been binned into 15° solar zenith angle intervals. When we applied the scattering function to data recorded when the solar zenith angle was very small, we saw that the function slightly underestimates the measured data. The scattering function therefore had to be slightly updated. See section A for details.

[9] Reflection ratios, $R_\perp$, that had been previously determined using CENA data had concentrated on the equatorial region and were computed using an isotropic angular distribution function [*Wieser et al.*, 2009; *Futaana et al.*, 2012]. For this study, we analyzed the neutral hydrogen measurements in the complete effective energy range (7 eV–3.52 keV) from the complete orbit (90°S–90°N, excluding the locations of magnetic anomalies) using the scattering function presented in section A. Since each angular sector provides us with an individual orbit data set and we have five angular sectors (view directions), the 153 orbits gave us 765 data sets to analyze. From these orbits, we had to exclude 48 data sets because they showed unrealistically high fluxes; i.e., during 16 orbits, the two sunward pointing sectors and the center sector were contaminated by ultraviolet light. The histogram of the $R_\perp$ values resulting for the remaining 717 data sets is shown in Figure 1a. Statistical analysis of the data yields a mean value of $R_\perp = 0.16$ (dashed line) and a standard deviation of 0.05 (dotted lines). These values are very close to the values also computed from the CENA data set limited to the equator region by *Futaana et al.* [2012] who reported a reflection ratio of $0.19^{+0.02}_{-0.03}$. When the data are divided into two energy ranges (cf. section 4), the low energy range (ENA energy < 30% of the impinging solar wind energy) contributes 0.097, and the high energy range (ENA energy > 30% of the impinging solar wind energy) contributes 0.063 to our result of $R_\perp = 0.16$. We also computed the reflection ratio for the nearside and the farside separately and found that the two values only differ by 0.002 which is well below the standard deviation of 0.05.

[10] We then sorted our reflection ratios by lunar longitude and by solar zenith angle (SZA), i.e., the angle under which the solar wind ions impinge onto the lunar surface, to see if the reflection ratio depends on either of them. Figure 1b shows the reflection ratio versus lunar longitude, and Figure 1c shows the reflection ratio versus solar zenith angle. The vertical lines depict the standard deviations, where available. As one can see from Figures 1b and 1c, there is no statistically significant correlation between the reflection ratio and the lunar longitude or the solar zenith angle. Thus, the scattering function f_S is implicitly validated. We conclude that the mean value of $R_\perp = (0.16 \pm 0.05)$ can be assumed to be the globally valid reflection ratio and can be used to calibrate global ENA maps.

4. High Energy and Low Energy ENA Albedo Maps

[11] To produce a global ENA albedo map, we analyzed the data orbit by orbit. We only created a map for the latitude interval (60°S–60°N) since the angular scattering function cannot be inverted in the polar regions. We chose to only plot the data recorded at 200 km and not the 100 km data, which results in a map with two longitude ranges where we have no data available: (0°E–30°E) and (0°W–40°W). In our analysis, we take advantage of the repetitive observation of the same area to improve statistics, which is only the case for the 200 km data. The 100 km data was obtained at the very beginning of the mission. In this first observations phase, out of caution, instead of running CENA steadily for longtime observations, CENA was, on average, only in

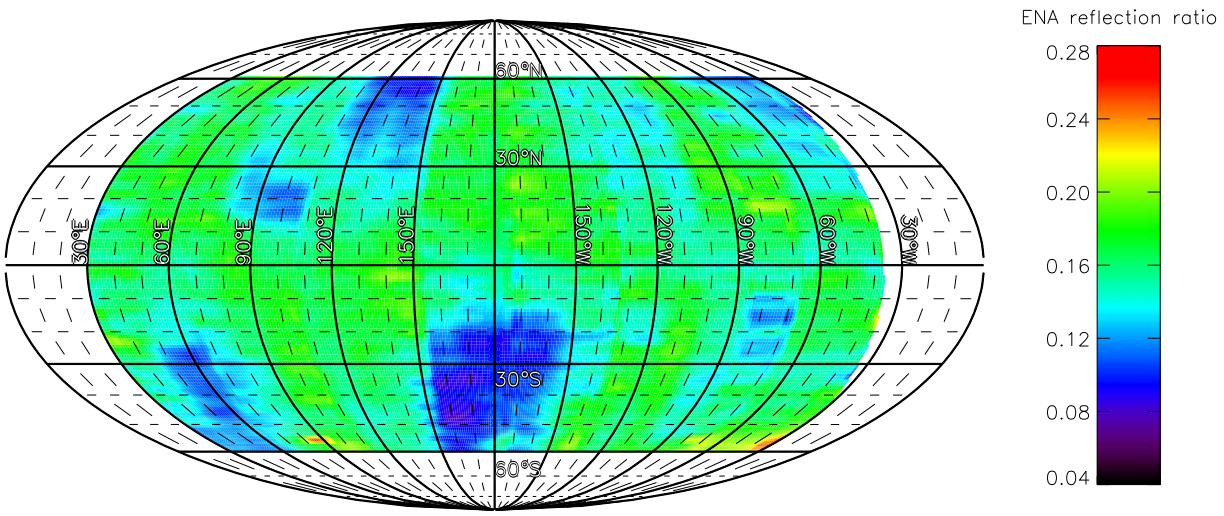

Figure 2. ENA reflection ratio map for CENA's complete energy range.

operation during three consecutive orbits per day. Since one orbit takes ∼2 h and two consecutive orbits are located ∼ 1° apart in longitude, the orbits from two consecutive days where located ∼ 18° apart. We therefore obtained only several isolated data strips and no continuously covered large areas during the 100 km orbit phase.

[12] For each orbit, we created two maps: a map of the expected flux (theoretical map) and a map of the measured flux (observation map). The theoretical map was calculated using the angular scattering function described in *Schaufelberger et al.* [2011] with the slight modification in the f_0 term as described in section A and using the global reflection ratio $R_\perp = 0.16$ derived in section 3. To create the observation map, the number of observed ENAs were distributed over the instrument's field of view projected onto the lunar surface. The resulting values were then multiplied with CENA's geometric factor and divided by the solar wind flux on the surface at the time of observation. The solar wind values were taken from the WIND spacecraft and time-shifted to the Moon's position compared to the WIND spacecraft location. We chose WIND data over SWIM data due to the data gaps in the latter, which would have forced us to omit some of the CENA orbits. Having computed the theoretical map and the observation map for each orbit, we added the different orbits' maps to compute a global theoretical map and a global observation map. Finally, the global observation map was divided by the global theoretical map to obtain a map showing local deviations from the global reflection ratio. Figure 2 shows the computed ENA reflection ratio map for CENA's complete energy range. If the Moon were a sphere with a homogeneous surface, then $R_\perp$ would be constant for the complete sphere. This is not the case in reality due to the lunar surface's heterogeneity, though, which is expressed in the map, where local deviations from the computed global reflection ratio of 0.16 are shown. Similarly, Figures 3a and 3b show two computed ENA reflection ratio maps for two different energy ranges (see discussion below). Figure 3c shows the effective exposure time for the two maps. The integration time to obtain one measurement was ∼4 s. For each measurement, these 4 s were multiplied with a two-dimensional Gaussian distribution, which covers the surface projected field of view of an angular sector and which has an integral of 1. This assigns each longitude/latitude configuration within the field of view a fraction of these 4 s in such a way that all exposed surface elements have a combined effective exposure time of 4 s. The effective exposure time in Figure 3c is the sum of all these fractions. Figure 3g and 3h show the average solar wind flux and velocity, respectively, under which the Moon was observed. In addition, we provide a slightly updated version of the map presented by *Mitchell et al.* [2008] showing the surface magnetic field strength measured by the Lunar Prospector Electron Reflectometer (Figure 3f) and a map showing the flux of deflected protons measured by SWIM/SARA and presented by *Lue et al.* [2011] (Figure 3e). Finally, Figure 3d shows a Clementine visible albedo map where eight regions of interest (see below) are encircled. Table 1 lists these regions and provides either the name and the center of the region (where available) or their longitudinal and latitudinal extent.

[13] As observed by *Wieser et al.* [2010], the signature of the minimagnetosphere located at the Gerasimovich crater (122°W, 22°S) is hardly visible in low energy ENAs (<100 eV), whereas it is well observed in high energy ENAs (in the range of 150 eV–600 eV). *Wieser et al.* [2010] also found that the ENAs have a distinct upper energy and that the solar wind particles lose on average more than 50% of their initial energy upon reflection from the lunar surface. The energy distribution of these ENAs was studied in detail by *Futaana et al.* [2012]. To increase the sensitivity to the imaging of magnetic anomalies, we also divided our energy range into a low energy interval (ENA energy <30% of the impinging solar wind energy) and a high energy interval (ENA energy >30% of the impinging solar wind energy). The threshold of 30% was chosen because it evenly divided the measured ENAs' energy spectrum into two groups which are shown in Figures 3a and 3b. The energy range of these two groups is rather wide, though. In the low and high energy map, thus, high flux artifacts are introduced in a few cases where we have very little effective exposure time. These artifacts are almost gone in the map over the full energy range. The robustness of each map can be derived from the

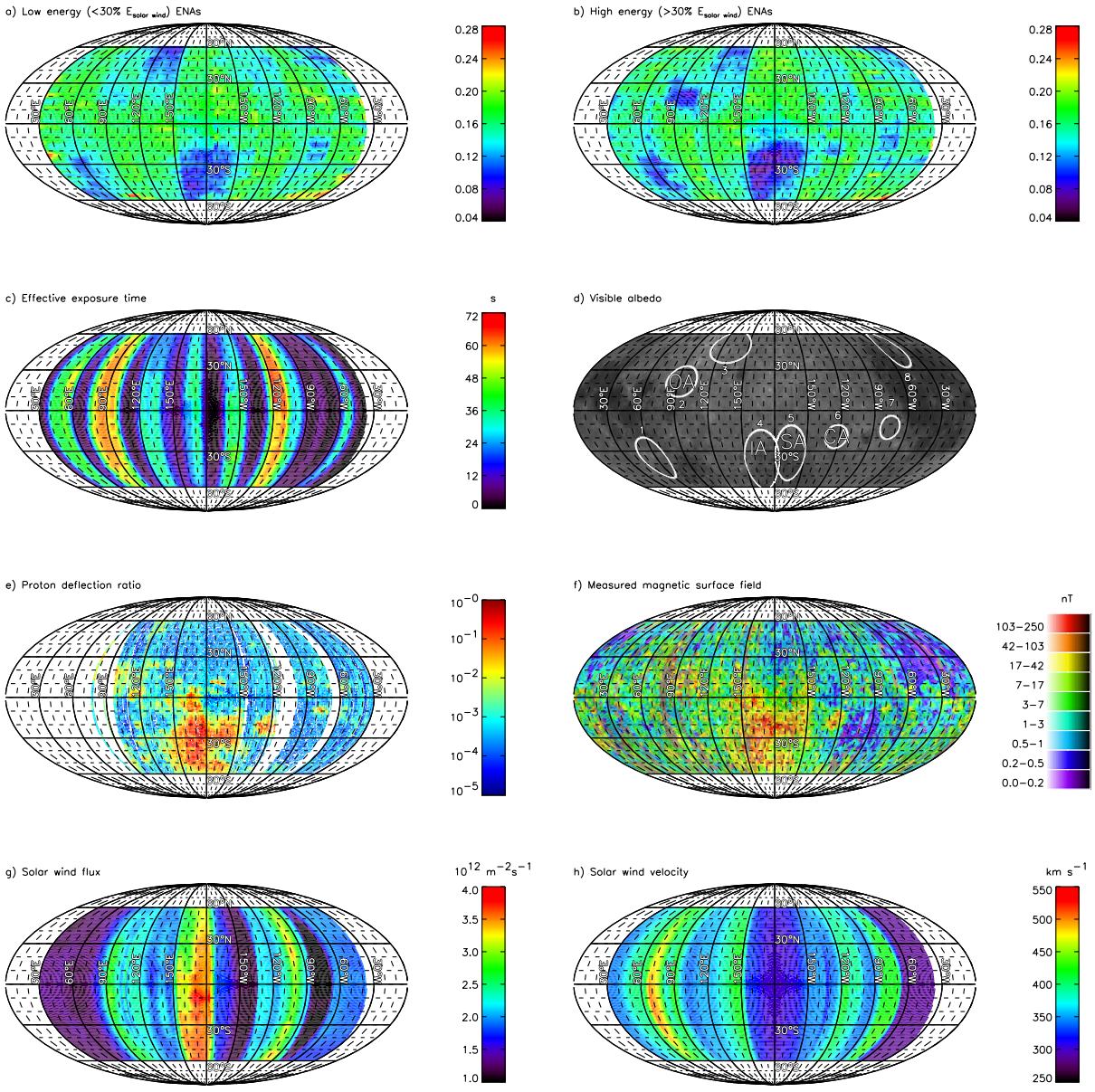

Figure 3. Neutral energetic hydrogen albedo maps of the lunar surface. Figure 3a was compiled using the low energy (ENA energy < 30% of the impinging solar wind energy) ENAs, whereas Figure 3b was compiled for the high energy (ENA energy > 30% of the impinging solar wind energy) ENAs measured by CENA. The ENA maps depict local deviations from the global reflection ratio, where a value of 1 designates no deviation from the global reflection ratio of $R_{\perp} = 0.16$, and a value smaller (larger) than 1 designates an area where less (more) particles were backscattered than the global average. Figure 3c shows the effective exposure time for each surface element used in the ENA maps. Figure 3d presents a lunar albedo map measured by Clementine with eight regions of interest encircled. Figure 3e shows the proton reflection ratio as measured by SWIM/SARA. This map is a slightly updated version of the map presented by *Lue et al.* [2011]. Figure 3f depicts also a slightly updated version of the lunar crustal magnetic field map measured by the Lunar Prospector Electron Reflectometer presented in *Mitchell et al.* [2008]. Figures 3g and 3h show the solar wind flux and velocity, respectively, during which the lunar surface was observed by CENA. In all eight panels, the locations of the four major magnetic anomalies are labeled: IA = Imbrium Antipode (4), SA = Serenitatis Antipode (5), CA = Crisium Antipode (6), and OA = Orientale Basin Antipode (2).

effective exposure time map. Due to the (usually) big number of observations and overlapping fields of view, a feature only shows up when it is present in several consecutive orbits and sectors' fields of view.

[14] In the high energy ENA map (Figure 3b), the mini-magnetospheres associated with the magnetic anomalies located at the Imbrium Antipode (Table 1, number 4), at the Serenitatis Antipode (Table 1, number 5), at the Crisium

Table 1. Regions of Interest and Either the Name and the Center of the Region (Where Available) or Their Longitudinal and Latitudinal Extent

Number	Designation	Location
1	-	(50°E–70°E, 20°S–60°S)
2	Orientale Basin Antipode	(87°E, 19°N)
3	-	(110°E–150°E, 40°N–60°N)
4	Imbrium Antipode	(164°E, 33°S)
5	Serenitatis Antipode	(162°W, 28°S)
6	Crisium Antipode	(122°W, 22°S)
7	-	(70°W–80°W, 10°S–20°S)
8	-	(40°W–60°W, 30°N–60°N)

Antipode (Table 1, number 6 = Gerasimovich crater), and at the Orientale Basin Antipode (Table 1, number 2) are clearly visible. There are three large-scale regions of reduced ENA flux (Table 1, numbers 1, 3, and 7) that could be caused by magnetic fields (see section 5 for a discussion on the uncertainty of the correlation). In addition, there is one large-scale reduced flux region (Table 1, number 8) for which we find no corresponding magnetic field feature.

[15] In the low energy range, the minimagnetosphere associated with the Imbrium and the Serenitatis Antipodes are also visible, but the latter is not as pronounced. The signatures of the minimagnetospheres associated with the Crisium Antipode and the Orientale Basin Antipode are not visible in this energy range, though. Identically to the high energy map, four additional pronounced large-scale ENA reflection reductions are visible at Table 1, numbers 1, 3, and 7 (with possible correlations in the magnetic field map) and Table 1, number 8 (with no correlation in the magnetic field map).

[16] In the high energy map, the abrupt boundary at the eastern edge of the Imbrium Antipode is most probably not physical but related to poor measurement statistics in coincidence with a factor of 2 difference in the solar wind flux across separate measurements.

5. Discussion

[17] Our obtained reflection value of $R_{\perp} = (0.16 \pm 0.05)$ agrees well with the previously determined lunar ENA albedo values. *McComas et al.* [2009] presented a first lunar global albedo value of ∼0.10 using IBEX data in the energy range 0.38–2.5 keV. More recent analysis of the IBEX data lead to a global albedo value of 0.09 ± 0.05 [*Rodríguez et al.*, 2012], which was later updated to 0.11 ± 0.06 [*Saul et al.*, 2013]. In a first analysis of the CH-1 data, *Wieser et al.* [2009] computed a lunar albedo value of 0.16–0.20 from three consecutive orbits centered around 8°W. *Futaana et al.* [2012] reported on a newer CH-1 data analysis, where data within ±30° of the equator from 52 orbits were used. These authors determine a local albedo value of $0.19^{+0.02}_{-0.03}$. Table 2 summarizes the lunar albedo values published until now. In this table, two energies are mentioned: E_{SW} denotes the solar wind energy at the time of the measurements, and E_{ENA} denotes the energy range within which the ENAs were measured. The IBEX reported values are all smaller than the CENA reported values. This difference arises from the two different observation setups: While IBEX conducts an integral measurement covering the illuminated lunar surface (which is about one fourth of the surface) from about 40 lunar radii away, CENA conducts many local measurements in low altitude of 100/200 km for ∼ 89% of the lunar surface.

[18] Our global ENA albedo maps show that the presence of a minimagnetosphere signature in the high but not in the low energy range is not only a feature of the Gerasimovich (= Crisium Antipode) anomaly but is also observed for the Orientale Basin Antipode. As suggested by *Halekas et al.* [2011] and *Lue et al.* [2011] based on Lunar Prospector and CH-1/SARA data, respectively, and measured by *Saito et al.* [2012] using MAP-PACE on Kaguya, static antimoonward electric fields exist over the magnetic anomalies on the lunar surface. These electric fields, together with the magnetic fields, not only deflect but also decelerate impinging solar wind ions. *Kallio et al.* [2012] confirmed the deceleration of impinging solar wind ions using a 3-D self-consistent hybrid model. Based on these findings, we interpret the difference in the low and high energy maps as follows: The impinging solar wind protons are slowed down and deflected upon interaction with the lunar minimagnetospheres. Whereas this produced partial depletions in the high energy range, the depletions in the low energy range are to some extent filled up again by slowed down protons from the high energy range. The magnetic anomaly signatures are therefore well pronounced in the high energy map, but not in the low energy map. This pattern of depletion in high energy ENAs and much less depletion in low energy ENAs is not observed at the large magnetic anomaly at South Pole-Aitken basin (Imbrium and Serenitatis Antipodes) where a depletion is observed both in high energy and low energy ENAs. This can be attributed to the much larger size of the magnetic anomaly (much larger than the proton gyroradius), or other features of the South Pole-Aitken basin like extreme topography, different geology, and different surface properties (e.g., low albedo).

[19] In section 4, we identified three regions (Table 1, numbers 1, 3, and 7) that might also be associated with magnetic anomalies. We are unsure of the true cause of these large-scale flux reductions for the following reasons. As mentioned above, the ENA flux reductions that correlate well with known magnetic anomalies are usually observed well in the high energy range but not so in the low energy

Table 2. Reported Lunar ENA Albedo Values

Reference	Source	Albedo	Region	E_{SW}	E_{ENA}
McComas et al. [2009]	IBEX-Hi/IBEX	∼ 0.10	Global	470–1140 eV	380–2500 eV
Rodríguez et al. [2012]	IBEX-Lo/IBEX	0.09 ± 0.05	Global	490–1635 eV	10–2000 eV
Saul et al. [2013]	IBEX-Lo/IBEX	0.11 ± 0.06	Global	490–1635 eV	10–2000 eV
Wieser et al. [2009]	CENA/CH-1	0.16–0.20	Local (∼ 8°W)	539–551 eV	38–652 eV
Futaana et al. [2012]	CENA/CH-1	$0.19^{+0.02}_{-0.03}$	Local (±30°N/S)	524–1494 eV	11–3300 eV
This paper	CENA/CH-1	0.16 ± 0.05	Global	340–1603 eV	11–2200 eV

range. The signatures of these two regions are about equally pronounced in both maps, though. In addition, at least for two of these locations (Table 1, numbers 1 and 3), there are other similarly strong magnetic anomalies located in the same orbit, i.e., same longitude but at different latitude. If the reduced flux is a true signature of a magnetic anomaly, then, under the same solar wind conditions, we should also be able to see other magnetic anomalies, which have about the same intensity and geometric extent as the one possibly identified. Finally, for the third location (Table 1, number 7), the reduced flux area seems rather large compared to the magnetic anomaly dimension in Figure 3f.

[20] There is one region (Table 1, number 8) which shows up in the low energy map as well as in the high energy map for which we find no corresponding magnetic field anomaly in the magnetic field map. There are of course other possible causes for these ENA flux reductions. They could, for example, be a result of mineralogical composition, physical surface features, topography, or geology features. We compared our maps to an elevation model based on Lunar Reconnaissance Orbiter data (Global Lunar Digital Terrain Model 100 m/pixel), a Clementine visible map, and two iron and titanium maps also based on Clementine data. Except for the South Pole-Aitken basin, which can be easily identified in all of these maps, we found no obvious correlation between our ENA maps and the topography, visible or geology maps, though.

[21] *Lue et al.* [2011] show a positive correlation between the magnetic field strength and the flux of deflected protons (see Figure 3e), while we observe an anticorrelation between the magnetic field strength and the reflected ENAs. Our map therefore appears to be an inverted image of the deflected proton map. Overall, our high energy map correlates very well with the map showing deflected protons. Note that in the ENA map as well as in the proton map, we see a signature of the same group of weak anomalies located at the Orientale Basin Antipode, which apparently act in a coherent manner to form a magnetosphere-like obstacle.

[22] Finally, we ran a 2-D correlation code to see if either the magnetic surface field or the magnetic field measured at an altitude of 30 km (e.g., presented by *Richmond and Hood* [2008]) correlates better with our high energy ENA albedo map. The analysis showed that our map correlates with either map equally well. In addition, the analysis showed that the ENA map correlates with either magnetic field map almost to the same extent as the two magnetic field maps correlate themselves. We also ran the 2-D correlation code with the ENA map, the visible albedo, the elevation, and the geology maps as input. The results showed that whereas our map correlates well with the magnetic field maps, it does not correlate well with either the visible albedo or the geology maps. This is probably due to strong features being present on the northern hemisphere of the lunar nearside in the albedo and geology maps but not in the ENA albedo map. The correlation is the least for the titanium map, which itself exhibits hardly any features on the lunar farside. The ENA albedo map correlates slightly better with the elevation map but not as well as with the magnetic field maps. It is noteworthy that whereas the ENA flux reduction and the magnetic anomaly at the Imbrium Antipode and the Serenitatis Antipode are located slightly north of the South Pole-Aitken basin, the albedo, elevation, and geology features associated with this basin are in comparison all located further south. These findings support the conclusion that the ENA flux reductions observed are signatures of magnetic anomalies.

6. Conclusion

[23] We computed a new global reflection ratio for perpendicular incidence of 0.16 ± 0.05 using CH-1/CENA data. This value agrees well with previously determined IBEX and CH-1/CENA albedo values and reduces the gap between the two reporting albedo groups (IBEX and CH-1/CENA).

[24] Using the complete data set measured by CH-1/CENA together with the new global reflection ratio, we were able to create the first global ENA albedo map covering $\sim 89\%$ of the lunar surface. Local variations in this map express the fact that the lunar surface is not a homogeneous sphere but exhibits local variations, which reduce the albedo to less than 0.08 and enhance the albedo to more than 0.25.

[25] To enhance the sensitivity to magnetic anomaly imaging, we divided the ENA energy range into a low energy interval (< 30% of the impinging solar wind energy) and a high energy interval (> 30% of the impinging solar wind energy). While most large magnetic anomaly features show up in the high energy map, they are much less, if at all, observable in the low energy map. There are three regions, which show up in the low and high energy map, that could possibly be associated with magnetic anomalies. Finally, there is one region of distinctly reduced ENA flux for which neither a magnetic anomaly nor another cause can be identified.

[26] Whereas ENA imaging is still an evolving observation technique, we are confident that it will prove to be a powerful tool in investigating different kinds of planetary surfaces, e.g., surfaces not protected by an atmosphere (e.g., Mercury and Ganymede) and planets exhibiting complex magnetic field structures (e.g., Mars and Ganymede).

Appendix A

[27] The backscattered ENA flux can be written in two different ways. On the one hand, based on geometric considerations, the reflected ENA flux J_{ENA} at a given solar zenith angle (SZA) is equal to the product of the incoming flux J_{SW}, the cosine of the solar zenith angle, and the reflection ratio $R_{\perp}$ for perpendicular incidence:

$$J_{\mathrm{ENA}}(\mathrm{SZA}) = J_{\mathrm{SW}} \cdot \cos(\mathrm{SZA}) \cdot R_{\perp}. \tag{A1}$$

[28] On the other hand, similar to the definitions by *Futaana et al.* [2006] and *Schaufelberger et al.* [2011], the directional ENA flux $j_{\mathrm{ENA}}(\mathrm{SZA}, \phi, \theta)$ can be described as the product of the solar wind flux J_{SW}, the reflection ratio for perpendicular incidence $R_{\perp}$, and the directional scattering function $f_S(\mathrm{SZA}, \phi, \theta)$:

$$j_{\mathrm{ENA}}(\mathrm{SZA}, \phi, \theta) = J_{\mathrm{SW}} \cdot f_S(\mathrm{SZA}, \phi, \theta) \cdot R_{\perp}, \tag{A2}$$

where ϕ is the scattering azimuth angle and θ is the scattering polar angle (0° = perpendicular to the surface). Note that while $j_{\mathrm{ENA}}(\mathrm{SZA}, \phi, \theta)$ denotes the ENA flux scattered in

one angular direction, $J_{ENA}(SZA)$ denotes the total ENA flux scattered in all directions, such that

$$\int j_{ENA}(SZA, \phi, \theta) \cdot \sin(\theta) d\phi d\theta = J_{ENA}(SZA). \quad (A3)$$

[29] Integrating over the two observation angles in equation (A2) gives

$$J_{ENA}(SZA) = J_{SW} \cdot \int f_S(SZA, \phi, \theta) \cdot \sin(\theta) d\phi d\theta \cdot R_{\perp}, \quad (A4)$$

[30] Combining equations (A1) and (A4), we get

$$\int f_S(SZA, \phi, \theta) \cdot \sin(\theta) d\phi d\theta = \cos(SZA). \quad (A5)$$

The integral of f_S over the hemisphere therefore has to be equal to the cosine of the SZA.

[31] According to *Schaufelberger et al.* [2011], the scattering function can be represented by a product of four separate functions, which describe the overall angular scattering profile:

$$f_S(SZA, \phi, \theta) = f_0(SZA) \cdot f_1(SZA, \phi) \cdot f_2(SZA, \phi) \cdot f_3(SZA, \theta). \quad (A6)$$

While f_0 describes the scattering function's overall amplitude, f_1 through f_3 describe three different features that were seen in the observation data and which are given by:

$$f_1(z_1, \phi) = z_1 \cdot \cos(2\phi) + (1 - z_1)$$
$$f_2(z_2, \phi) = z_2 \cdot \cos(\phi) + (1 - z_2)$$
$$f_3(z_3, \theta) = (1 - \frac{z_3}{90°}) \cdot \sin(\theta + z_3) + \frac{z_3}{90°}, \quad (A7)$$

where ϕ is the azimuth scattering angle, θ is the polar scattering angle, and SZA is the solar zenith angle. The parameters for equation (A7) are

$$z_1(SZA) = (0.30 \cdot SZA + 1.72°) \cdot \left(\frac{\pi}{180°}\right)$$
$$z_2(SZA) = 0.24 \cdot \cos(74.48° - 1.52 \cdot SZA)$$
$$z_3(SZA) = 90° - 1.03 \cdot SZA.$$

Since, the integral of f_S has to be equal to the cosine of the solar zenith angle, and f_0 is only a function of the solar zenith angle and not of the observation angles, equations (A4) and (A6) lead to

$$f_0(SZA) = \frac{\cos(SZA)}{\int f_1(SZA, \phi) \cdot f_2(SZA, \phi) \cdot f_3(SZA, \theta) d\Omega^2}, \quad (A8)$$

which gives, written out

$$f_0(SZA) = \cos(SZA)/(0.074 \cdot (SZA - 3.23) \cdot (2 \cdot SZA \cdot \cos(1.03 \cdot SZA) + SZA \cdot \sin(1.03 \cdot SZA) \cdot \pi - 4 \cdot (SZA - 1.53)) \cdot (\cos(1.52 \cdot SZA - 1.30) - 4.17)),$$

with SZA given in rad.

[32] Figure A1a shows $f_0(SZA)$ as defined in equation (A8) and $f_0(SZA)$ as defined in *Schaufelberger et al.* [2011]. In *Schaufelberger et al.* [2011], a discrete integration was applied, and the normalization was different to the analytic form given in equation (A8). We therefore normalized each function to one to make it easier for the reader to compare the shapes of the curves. When we plotted the two $f_0(SZA)$s, we saw that the forms are very similar but that the maximum of $f_0(SZA)$ is shifted from SZA = 34° [*Schaufelberger et al.*, 2011] to SZA = 29° (equation (A8)). We are confident that this difference of 5° is acceptable, since the angular binning in the data analysis in *Schaufelberger et al.* [2011] was 15°, which is much larger than the difference. The main difference in these two forms is due to this shift of 5°. If we shift one of the two forms by 5° in the respective direction, then the two forms are almost identical (see Figure A1b where $f_0(SZA)$ from equation (A8) was shifted by 5°). As mentioned in the text, the main problem with the original function was that it underestimates the reflection for small SZAs. This is not the case anymore for the new function, which is nevertheless very similar to the $f_0(SZA)$ presented in *Schaufelberger et al.* [2011].

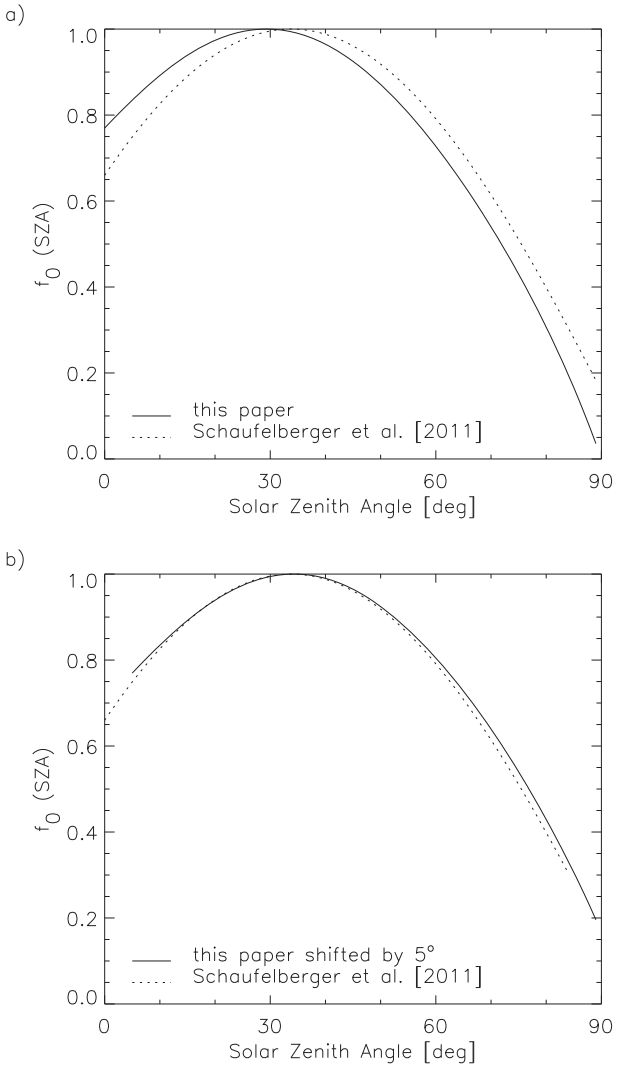

Figure A1. $f_0(SZA)$ as defined in equation (A8) and $f_0(SZA)$ as defined in *Schaufelberger et al.* [2011]. Figure A1a depicts the functions as written, whereas in Figure A1b, $f_0(SZA)$ from equation (A8) was shifted by 5°. In both panels, for easier comparison, both functions were normalized for one.

[33] **Acknowledgments.** A. Vorburger and P. Wurz gratefully acknowledge the financial support by the Swiss National Science Foundation. The authors thank Jasper Halekas who provided us with the slightly

updated version of the magnetic surface field map presented by *Mitchell et al*. [2008]. The authors would also like to thank Paul Spudis who told us where we could find the latest topography and geology maps. Solar wind parameters from the WIND spacecraft were used as a reference for this study. The authors thank K.W. Ogilvie (NASA/GSFC) and A.J. Lazarus (MIT) for providing WIND data. The efforts at Space Physics Laboratory, Vikram Sarabhai Space Centre are supported by the Indian Space Research Organisation (ISRO).

[34] Philippa Browning thanks the reviewers for their assistance in evaluating this paper.

References

Barabash, S., et al. (2009), Investigation of the solar wind-Moon interaction onboard Chandrayaan-1 mission with the SARA experiment, *Curr. Sci.*, *96*(4), 526–532.

Bhardwaj, A., S. Barabash, Y. Futaana, Y. Kazama, K. Asamura, R. Sridharan, M. Holmström, P. Wurz, and R. Lundin (2005), Low energy neutral atom imaging on the Moon with the SARA instrument aboard Chandrayaan-1 mission, *J. Earth. Syst. Sci.*, *114*(6), 749–760, doi:10.1007/BF02715960.

Blewett, D., E. Coman, R. Hawke, J. Gillis-Davis, M. Purucker, and C. Hughes (2011), Lunar swirls: Examining crustal magnetic anomalies and space weathering trends, *J. Geophys. Res.*, *116*, E02002, doi:10.1029/2010JE003656.

Crider, D., and R. Vondrak (2002), Hydrogen migration to the lunar poles by solar wind bombardment of the moon, *Adv. Space Res.*, *30*(8), 1869–1874, doi:10.1016/S0273-1177(02)00493-3.

Futaana, Y., S. Barabash, M. Holmström, and A. Bhardwaj (2006), Low energy neutral atoms imaging of the moon, *Planet. Space Sci.*, *54*, 132–143, doi:10.1016/j.pss.2005.10.010.

Futaana, Y., S. Barabash, M. Wieser, M. Holmström, C. Lue, P. Wurz, A. Schaufelberger, A. Bhardwaj, M. Dhanya, and K. Asamura (2012), Empirical energy spectra of neutralized solar wind protons from the lunar regolith, *Geophys. Res. Lett.*, *117*, E05005, doi:10.1029/2011JE004019.

Goswami, J., and M. Annadurai (2009), Chandrayaan-1: India's first planetary science mission to the moon, *Curr. Sci.*, *96*(4), 486–491.

Halekas, J., Y. Saito, G. Delory, and W. Farrell (2011), New views of the lunar plasma environment, *Planet. Space Sci.*, *59*, 1681–1694.

Kallio, E., et al. (2012), Kinetic simulations of finite gyroradius effects in the lunar plasma environment on global, meso, and microscales, *Planet. Space Sci.*, *74*, 164–155, doi:10.1016/j.pss.2012.09.012.

Kazama, Y., S. Barabash, M. Wieser, K. Asamura, and P. Wurz (2007), Development of an LENA instrument for planetary missions by numerical simulations, *Planet. Space Sci.*, *55*, 1518–1529, doi:10.1016/j.pss.2006.11.027.

Lue, C., Y. Futaana, S. Barabash, M. Wieser, M. Holmström, A. Bhardwaj, M. B. Dhanya, and P. Wurz (2011), Strong influence of lunar crustal fields on the solar wind flow, *Geophys. Res. Lett.*, *38*, L03202, doi:10.1029/2010GL046215.

McCann, D., S. Barabash, H. Nilsson, and A. Bhardwaj (2007), Miniature ion mass analyser, *Planet. Space Sci.*, *55*(9), 1190–1196, doi:10.1016/j.pss.2006.11.020.

McComas, D., et al. (2009), Lunar backscatter and neutralization of the solar wind: First observations of neutral atoms from the moon, *Geophys. Res. Lett.*, *36*, L12104, doi:10.1029/2009GL038794.

Mitchell, D., J. Halekas, R. Lina, S. Freya, L. Hood, M. Acuña, and A. Binder (2008), Global mapping of lunar crustal magnetic fields by Lunar Prospector, *Icarus*, *194*, 401–409, doi:10.1016/j.icarus.2007.10.027.

Richmond, N., and L. Hood (2008), A preliminary global map of the vector lunar crustal magnetic field based on Lunar Prospector magnetometer data, *J. Geophys. Res.*, *113*, E02010, doi:10.1029/2007JE002933.

Rodríguez, D., L. Saul, P. Wurz, S. Fuselier, H. Funsten, E. Möbius, and D. McComas (2012), IBEX-Lo observations of energetic neutral hydrogen atoms originating from the lunar surface, *Planet. Space Sci.*, *60*, 297–303, doi:10.1016/j.pss.2011.09.009.

Saito, Y., et al. (2010), In-flight performance and initial results of plasma energy angle and composition experiment (PACE) on SELENE (KAGUYA), *Space Sci. Rev.*, *154*, 265–303, doi:10.1007/s11214-010-9647-x.

Saito, Y., M. Nishino, M. Fujimoto, T. Yamamoto, S. Yokota, H. Tsunakawa, H. Shibuya, M. Matsushima, H. Shimizu, and F. Takahashi (2012), Simultaneous observation of the electron acceleration and ion deceleration over lunar magnetic anomalies, *Earth Planets Space*, *64*, 83–92, doi:10.5047/eps.2011.07.011.

Saul, L., P. Wurz, A. Vorburger, D. Rodríguez, S. Fuselier, D. McComas, E. Möbius, S. Barabash, H. Funsten, and P. Janzen (2013), Solar wind reflection from the lunar surface: The view from far and near, *Planet. Space Sci.*, in press.

Schaufelberger, A., P. Wurz, S. Barabash, M. Wieser, Y. Futaana, M. Holmström, A. Bhardwaj, M. Dhanya, R. Sridharan, and K. Asamura (2011), Scattering function for energetic neutral hydrogen atoms off the lunar surface, *Geophys. Res. Lett.*, *38*, L22202, doi:10.1029/2011GL049362.

Vorburger, A., P. Wurz, S. Barabash, M. Wieser, Y. Futaana, M. Holmström, A. Bhardwaj, and K. Asamura (2012), Energetic neutral atom observations of magnetic anomalies on the lunar surface, *J. Geophys. Res.*, *117*, A07208, doi:10.1029/2012JA017553.

Wieser, M., S. Barabash, Y. Futaana, M. Holmström, A. Bhardwaj, R. Sridharan, M. Dhanya, P. Wurz, A. Schaufelberger, and K. Asamura (2009), Extremely high reflection of solar wind protons as neutral hydrogen atoms from regolith in space, *Planet. Space Sci.*, *57*, 2132–2134, doi:10.1016/j.pss.2009.09.012.

Wieser, M., S. Barabash, Y. Futaana, M. Holmström, A. Bhardwaj, R. Sridharan, M. Dhanya, A. Schaufelberger, P. Wurz, and K. Asamura (2010), First observation of a mini-magnetosphere above a lunar magnetic anomaly using energetic neutral atoms, *Geophys. Res. Lett.*, *37*, L05103, doi:10.1029/2009GL041721.

Wurz, P. (2000), Detection of energetic neutral particles, in *The Outer Heliosphere: Beyond the Planets*, edited by K. Scherer, H. Fichtner, and Marsch, E., pp. 251–288, Copernicus Gesellschaft e.V., Katlenburg-Lindau, Germany.

Wurz, P. (2005), Solar wind composition, in *The Dynamic Sun: Challenges for Theory and Observations*, edited by D. Danesy, S. Poedts, A. De Groof, and J. Andries, vol. 5.2, pp. 1–9, 11-16 September 2005, Leuven, Belgium, (ESA SP-600, December 2005), ESA Publications Division, ESTEC, Noordwijk, The Netherlands.

Wurz, P., and H. Lammer (2003), Monte-Carlo simulation of Mercury's exosphere, *Icarus*, *164*, 1–13, doi:10.1016/S0019-1035(03)00123-4.

Wurz, P., U. Rohner, J. A. Whitby, C. Kolb, H. Lammer, P. Dobnikar, and J. A. Martín-Fernández (2007), The lunar exosphere: The sputtering contribution, *Icarus*, *191*, 486–496, doi:10.1016/j.icarus.2007.04.034.

Zimmerman, M., W. Farrell, T. Stubbs, J. Halekas, and T. Jackson (2011), Solar wind access to lunar polar craters: Feedback between surface charging and plasma expansion, *Geophys. Res. Lett.*, *38*, L19202, doi:10.1029/2011GL048880.